Mild acidolysis-assisted hydrothermal carbonization of lignin for simultaneous preparation of green and blue fluorescent carbon quantum dots

SCHOLARONE™
Manuscripts

1
2
3
4
5
6
7
8
9
10
11
12
13
14
15
16
17
18
19
20
21
22
23
24
25
26
27
28
29
30
31
32
33
34
35
36
37
38
39
40
41
42
43
44
45
46

Graphic abstract

Mild acidolysis-assisted hydrothermal carbonization of lignin for simultaneous preparation of green and blue fluorescent carbon quantum dots

Lingli Zhu[a], Dekui Shen[a,*] Kai Hong Luo[b]

[a] Key Laboratory of Energy Thermal Conversion and Control of Ministry of Education, School of Energy and Environment, Southeast University, Nanjing 210096, PR China.

[b] Department of Mechanical Engineering, University College London, London WC1E7JE, U.K.

*Corresponding Author

E-mail address: 101011398@seu.edu.cn (D. Shen)

Abstract: Biomass waste is a renewable, low-cost and green feedstock for the production of carbon quantum dots (CQDs), but its high-efficiency utilization remains a challenge. Here, we report a mild acidolysis-assisted hydrothermal strategy toward the simultaneous preparation of green and blue fluorescent CQDs from lignin. The synthetic processes involve the acid hydrolysis of lignin followed by the hydrothermal carbonization of its supernatant and solid residue, respectively. The fluorescence mechanism of the two CQDs is elucidated through the investigation of their structure, chemical composition and optical properties combined with quantum chemistry calculations. Their formation mechanism is also explored, nuclear magnetic resonance (NMR) data demonstrates that green CQDs are derived from the side chain scission of lignin by the bottom-up method, while blue CQDs inherit the aromatic bulk of lignin via the top-down method. The optimal yield of two CQDs can be achieved as 30.6% for green CQDs and 15.2% for blue CQDs by adjusting the acidolysis temperatures from 30 to 110 ℃. This comprehensive strategy promotes the high-efficiency conversation of biomass into CQDs and

provides a theoretical basis for exploring the fluorescence mechanism and formation mechanism of CQDs.

Keywords: Lignin, Acidolysis, Hydrothermal carbonization, Simultaneous preparation, Carbon quantum dots, Mechanism

1. Introduction

Energy crisis, overconsumption of non-renewable resources along with the rapid deterioration of the natural environment are global challenges that humanity is confronted with [1, 2]. In this case, the conversion of biomass waste (agricultural residues, food waste, municipal solid waste, etc.) into high-value materials takes great potential to alleviate these issues due to its clean, abundant, renewable, and environmentally friendly raw material [3, 4]. Biomass waste with a high carbon content of 45-55 wt% has been utilized to produce novel carbon-based materials such as graphene [5], carbon nanotubes (CNTs) [6], carbon nanofiber (CNFs) [7], carbon nano onion (CNOs) [8], porous carbon (PCs) [9] and carbon quantum dots (CQDs) [10]. Thermochemical conversion of biomass has been intensively researched and several techniques are developed, such as pyrolysis, gasification, liquefaction, and hydrothermal carbonization [11, 12]. Among them, hydrothermal carbonization is a widely used technique for the thermochemical decomposition of biomass with water as the medium. The epoxy bonds in carbon-containing raw materials are easily broken under high temperature and high pressure, so the bulk carbon materials are cut into small particles to acquire target products [13, 14]. Hydrothermal carbonization has superior characteristics of mild heating temperature (around 200 ℃), low energy consumption, cost-effectivity, and flexible operation [15, 16]. To date, biomass-derived carbon nanomaterials via hydrothermal carbonization have been a hot topic in materials science

and engineering.

CQDs, as a rising star of carbon nanomaterial, have gained tremendous attention due to their unique physicochemical properties including tunable fluorescence emission, good water solubility, excellent chemical stability, low toxicity, and high conductivity [17, 18]. For their low cost, renewability, and environmental friendliness, biomass-derived CQDs prepared by hydrothermal carbonization show great promise for the sustainable development of applications in bioimaging, sensing, catalysis, and drug delivery, light-emitting diodes, and anti-counterfeiting [10, 19]. Currently, a variety of natural biomasses such as microalgae [20], fresh grass [21], cabbage [22], chia seeds [23], chitosan [24], etc. are used to prepare CQDs by a simple one-step hydrothermal method. Unfortunately, most biomass-derived CQDs are produced in extremely low yields (less than 10%), severely limiting their commercial applications. Since the one-step hydrothermal reaction is uncontrollable, a large number of hydrochar are often produced during the process of CQDs formation. As a kind of macroscopic carbon material, hydrochar has great potential for the further synthesis of CQDs [20, 25, 26]. Zhou et al. [27] used hydrochar from food waste via hydrothermal carbonization as a carbon-rich precursor and successfully prepared multicolour CQDs by refluxing HNO_3 and H_2SO_4. Zhao et al. [28] prepared CQDs from hemicellulose-based hydrochar and $NaOH/O_2$ by a hydrothermal method, and obtained yields of 19.6% ~ 29.1% by adjusting different hydrothermal temperatures. Jing et al. [13] obtained an ultrahigh CQDs yield of 40.1% from glucose-based hydrochar through $NaOH/H_2O_2$ treatment. The formation mechanism of biomass-derived CQDs was preliminarily speculated to involve hydrolysis, dehydration, decarboxylation, aromatization, and recondensation based on the literature and limited characterization. It can be found that using hydrochar to prepare CQDs is

obviously beneficial to improve the efficiency of biomass conversion. However, the use of strongly corrosive acids or alkalis adds risk to the environment and human health. In addition, the fluorescence mechanism is unclear and formation mechanism of CQDs from biomass is rarely investigated. Herein, more work is required for the highly efficient conversion of whole biomass into carbon materials by a green and facile method, as well as the exploration of the fluorescence mechanism and formation mechanism.

In this work, a facile and efficient strategy is proposed to simultaneously produce green and blue CQDs from lignin and mild organic acid (o-aminobenzenesulfonic acid) by acidolysis-assisted hydrothermal carbonization (Figure 1). Two kinds of CQDs are obtained from the supernatant and solid residue of acid hydrolyzed lignin, respectively, and their physicochemical properties are investigated. The fluorescence mechanism is clearly revealed according to their different structure, composition and optical properties combined with quantum chemistry calculations. The formation mechanism of two CQDs from lignin in the synthetic process is discussed in-depth through a systematic characterization analysis of raw materials, intermediates, and target products. It hopes to promote the large-scale and green production of carbon nanomaterials from biomass and offer new insight into the comprehensive utilization strategy of biomass.
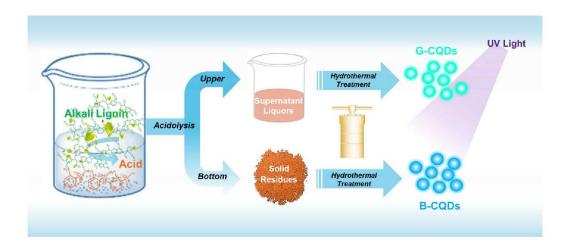
Figure 1. Scheme of the synthetic route of green and blue CQDs from alkali lignin.

2. Experimental section

2.1 Materials and chemicals

Alkali lignin (AL, ≥96%) with low content of sulfur was acquired from Sigma-Aldrich (China). O-aminobenzenesulfonic acid (99%) was purchased from Bidepharm (China). Deionized (DI) water was used throughout this experiment. The dialysis bags with a retained molecular weight of 1000 Da were provided by Viskase (USA). The PTFE microporous filter membranes with pore diassssss of 0.1 μm, respectively were obtained by Jinteng (Tianjin, China). All reagents are of analytical grade and used without further purification.

2.2 Synthesis of green and blue fluorescent CQDs

O-aminobenzenesulfonic acid (0.3 g) was dispersed in 30 mL of DI water and AL (0.3 g) was added slowly with manual stirring. The mixed solution was then heated in a water bath at different temperatures (30, 50, 70, 90, 110 °C) for 1 h with continuous stirring at 350 rpm. The solution after the acidolysis reaction was separated by a high-speed centrifuge at 12,000 rpm. The obtained supernatant liquids (SLs) and solid residues (SRs) were used for further preparation of two kinds of lignin-derived CQDs, respectively. The SLs and SRs dispersed in

30 mL of DI water were transferred into a 50 mL Teflon-lined stainless autoclave and kept at 200 °C for 12 h, respectively. After naturally cooling to room temperature, the obtained products containing water-soluble CQDs were filtrated by vacuum microporous suction filtration (microporous fiber membrane of 0.10 μm). The filtrate was further dialyzed in a dialysis bag (1000 Da) for 2 days and then freeze-dried at -60 °C into CQDs powder. The CQDs prepared from the supernatant and solid residue were denoted as G-CQDs and B-CQDs, respectively. The yield of G-CQDs and B-CQDs was determined by using the following Equations (1) and (2):

$$\text{Y}_{G-CQDs}(wt\%) = (W_{G-CQDs}/W_r) \times 100\% \tag{1}$$

$$\text{Y}_{B-CQDs}(wt\%) = (W_{B-CQDs}/W_r) \times 100\% \tag{2}$$

where Y_{G-CQDs} and Y_{B-CQDs} represent the yield of B-CQDs and B-CQDs, W_{G-CQDs} and W_{B-CQDs} represent the weight of B-CQDs and B-CQDs, W_r represents the weight of raw materials (AL and o-aminobenzenesulfonic acid).

2.3 Characterization of lignin-derived CQDs

The detailed morphology was observed using a high-resolution transmission electron microscope (HR-TEM, Tecnai G2 F20, FEI, USA). The graphitized structure was recorded by a Micro-Raman spectrometer with InGaN laser excitation at 532 nm (DXR 2xi, ThermoFisher, USA). The chemical composition was characterized by a Fourier transform infrared spectrometer (FT-IR, Nicolet Is5, ThermoFisher, USA) and an X-ray photoelectron spectrometer (XPS, K-Alpha, ThermoFisher, USA). The ^{13}C-^{1}H chemical environment was measured by the two-dimensional heteronuclear singular quantum correlation nuclear magnetic resonance spectrometer (2D-HSQC NMR, Avance III 600 MHz, Bruker, Germany) with the

dispersant of dimethyl sulfoxide-d6 (DMSO) for AL and deuterium oxide (D_2O) for LNPs and CQDs. The optical properties were measured by an ultraviolet−visible spectrophotometer (UV-vis, UV-5200, Yuanxi, China) and a fluorescence spectrophotometer (Cary Eclipse, Agilent, USA). The time-resolved PL spectra were acquired from a steady/transient state fluorescence spectrophotometer (TRPL, FLS1000, Edinburgh, UK).
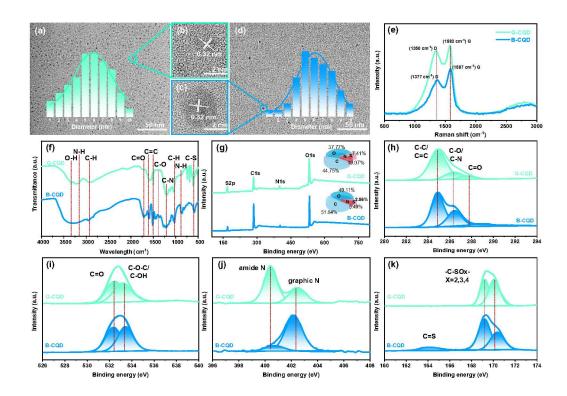
3. Results and discussion

3.1 Morphology and structure of G-CQDs and B-CQDs

The CQDs obtained at the acidolysis temperature of 90 °C are selected as typical for the investigation and characterization. The TEM and HR-TEM images in Figure 2a-d clearly show the micromorphology of resultant G-CQDs and B-CQDs. They are both uniformly dispersed in aqueous solution with an average particle size of 4.76 and 5.55 nm, and G-CQDs are more densely dispersed than B-CQDs. The HR-TEM images of the two CQDs show high crystallinity and the same lattice fringe with a spacing of 0.34 nm corresponding to the graphene (002) [29, 30]. The graphitization of the two CQDs is further confirmed by Raman spectra (Figure 2e). There are two distinct peaks at 1350/1377 cm^{-1} (D peak) and 1583/1587 cm^{-1} (G peak), representing the vibrations of disordered sp^3 and graphitized sp^2 carbon [31]. The intensity ratios (I_D/I_G) of G-CQDs and B-CQDs are 2.63 and 1.85, respectively, indicating that the degree of graphitization of B-CQDs is higher than that of G-CQDs [18, 32]. This confirms that there is a more conjugated graphene structure in B-CQDs in comparison with G-CQDs [4, 33].

The chemical composition and surface functional groups of CQDs are characterized by FTIR and XPS. As shown in Figure 2f, the broad peaks in the range of 3000-3600 cm^{-1} in FTIR spectra are assigned to O-H/N-H stretching vibrations. The peaks located at 2879, 1732, 1515-

1595, and 1349 cm^{-1} represent the saturated C-H, C=O, C=C, and C-O functional groups, respectively [34]. The peaks observed at 1300, 885 and 614 cm^{-1} reveal the presence of C-N, N-H, and C-S functional groups [35, 36]. These results suggest the successful co-doping of N and S both in G-CQDs and B-CQDs, which can be further confirmed by XPS analysis. The XPS survey spectra show the two CQDs have four prominent peaks at 284.8, 532.1, 400.1, and 168.1 eV corresponding to C 1s, O 1s, N 1s, and S 2p respectively (Figure 2g). The high-resolution XPS spectra of C 1s, O 1s, N 1s, and S 2p are displayed in Figure 2h-k. The C 1s spectra can be fitted with three peaks at 284.8, 286.2, and 287.8 eV, corresponding to sp^2 carbon (C-C/C=C), and sp^3 carbon (C-O/C-N), and carbonyl groups (C=O). The O 1s spectra can be deconvoluted into two peaks at 532.4 and 533.3 eV for C=O and C−O-C/C-OH. The N 1s spectra show two peaks at 400.2 and 402.3 eV for amide N and graphic N groups. The S 2p spectra have two peaks at 164.3, 169.2, and 170.1 eV corresponding to C-S and C-SO$_x$ groups [34-36]. Furthermore, the quantitative analysis data of XPS for G-CQDs and B-CQDs demonstrates that the total content of N and S doped in G-CQDs is much higher than that in B-CQDs, while B-CQDs possess a higher C content of 51.84%. According to the above structural analysis of Raman, FT-IR, and XPS, it can be concluded that the two lignin-derived CQDs have extensive conjugated sp^2 domains in the carbon core along with some heteroatoms (O, N and S) doping on the surface. It is worth noting that B-CQDs have a higher degree of graphitization, while G-CQDs have more surface defects.
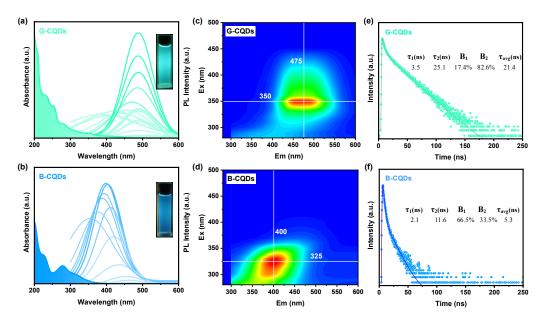
Figure 2. Morphology and structures of CQDs. (a-d) TEM image and HR-TEM image (inset: diameter distribution), (e) Raman, (f) FTIR, (g) XPS survey and high-resolution XPS spectra of (h) C 1s, (i) O 1s, (j) N 1s, and (k) S 2p of G-CQDs and B-CQDs.

3.2 Optical properties of G-CQDs and B-CQDs

The optical properties of fluorescent G-CQDs and B-CQDs are further analyzed. As presented in Figure 3a, the UV-vis absorption spectra of G-CQDs show two adsorption peaks at 233, 256 nm and a weak one at 356 nm, with an optical absorption edge at ~500 nm. The UV-vis spectra of B-CQDs show two strong adsorption peaks at 228, 280 nm and a very weak one at 320 nm (Figure 3b). The first two peaks below 300 nm are attributed to the $\pi-\pi^*$ transition of C=C in the carbon core, while the other peak over 300 nm is corresponding to the n$-\pi^*$ transition of C=O/C=N on the surface of CQDs [33, 37]. The UV$-$vis spectrum of G-CQDs exhibits stronger absorbance over 300 nm than that of B-CQDs, which implies more abundant surface defects introduced by heteroatoms doping in G-CQDs. It is consistent with the above

results of Raman, FTIR, and XPS [18]. As for the photoluminescence (PL) performance of CQDs, the PL emission spectra of G-CQDs and B-CQDs present the up-conversion and excitation-dependent behavior excited in the range of 280-500 nm. It can be attributed to the differences in surface heteroatom functional groups and sizes. The excitation-emission matrix spectra in Figure 3c, d show that the maximum excitation-emission of G-CQDs and B-CQDs are centered at (350, 475) and (325, 400) nm, which are corresponding to green and blue fluorescence color, respectively.

Figure 3. Optical properties of CQDs. (a, b) UV-vis absorption spectra and PL emission spectra excited by various incident lights progressively from 280 to 500 nm with a 10 nm increment (inset: photograph under UV irradiation). (c, d) Excitation-emission matrix spectra. (e, f) Time-resolved PL decay curves of G-CQDs and B-CQDs.

3.3 Fluorescence mechanism of G-CQDs and B-CQDs

As well known, the PL behavior of CQDs depends on the comprehensive effect of carbon core and surface defects state. The fluorescence mechanism of G-CQDs and B-CQDs is proposed in Figure 4a, b, various energy levels are associated with the incorporation of the

oxygen, nitrogen, and/or sulfur-containing functional groups of CQDs. These defects produced by oxidation, nitration, and/or sulfonation as capture centers of excitons give rise to the surface-state-related fluorescence [34, 38]. In this study, several distinct defect states induced by oxygen, nitrogen, and sulfur-containing functional groups are generated in G-CQDs and B-CQDs, leading to the additional energy levels (n-π* transitions) between π and π* transition [10]. The O-related functional groups, especially C=O with the strong electron-accepting property are considered to be chromophores [39, 40]. The N, S related groups are identified as auxochrome groups, the isolated n electrons of which and π electrons of the carbon ring are almost coplanar [41-43]. The efficient separation of electrons and holes within the n-π* gap can be adjusted by varying the content of O, N, and S doping [34, 35, 44, 45]. The additional n-π* transitions result in multiple radiation recombination paths back to the ground state, thereby leading to the red-shift of the emission wavelength from B-CQDs to G-CQDs [18, 46]. In addition, the related PL quantum yield (QYs) of G-CQDs (23.7%) is superior to that of B-CQDs (5.2%), which is considered to be attributed to the increased doping content of nitrogen [10, 31, 47].

The complicated fluorescence mechanism of CQDs is explored in depth by theoretical calculations. To investigate the size-dependent effect, four CQDs models with increasing benzene ring numbers are designed and their highest occupied molecular orbital (HOMO) and lowest unoccupied molecular orbital (LUMO) energy levels and bandgaps are calculated. As shown in Figure 5a, the bandgap narrows significantly from 4.03 to 0.82 eV as the number of benzene rings increases from 7 to 24, which indicates that the larger sp^2 conjugated structure of CQDs contributes to the gradual red-shift of fluorescence emission [18, 48]. CQDs models composed of seven benzene rings and different oxygen-containing, nitrogen-containing and sulfur -containing functional groups are also designed. According to Figure 5b, the bandgap slightly decreases from 3.83 to 3.55 eV as the number of hydroxyl groups (-OH) increases from 3 to 6, 10, while the bandgap sharply decreases from 3.77 to 2.78 eV in the addition of carboxyl groups (-COOH). The n electrons of -C=O lower both HOMO and LUMO energy levels, leading to a reduction in the bandgap and a red shift of fluorescence emission [33, 37]. As presented in Figure 5c and 5d, although the bandgap does not change in the addition of amine groups (-NH_2) or sulfonic groups (-SO_3H), which is narrower than that without substituents. The bandgap increases in the addition of -C-N groups and gradually decreases in the addition of –

C-S groups. The theoretical calculation results demonstrate that larger sp^2 conjugated structure and increased surface oxygen or sulfur -containing functional groups (especially -C=O and -C-S groups) contribute to a narrowing of the bandgap and a red-shift of the fluorescence wavelength, which agrees well with the experimental results. Compared with B-CQDs, G-CQDs contain more oxygen- or sulfur-containing functional groups on their surface, resulting in a shift in fluorescence emission from blue to green, while the fluorescence intensity is dependent on the nitrogen-containing functional groups. The quantitative results above conduce to reveal the ambiguous fluorescence mechanism of CQDs illustrated in this work.
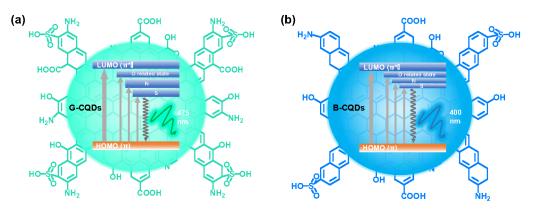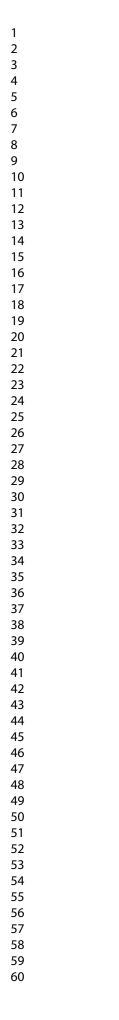

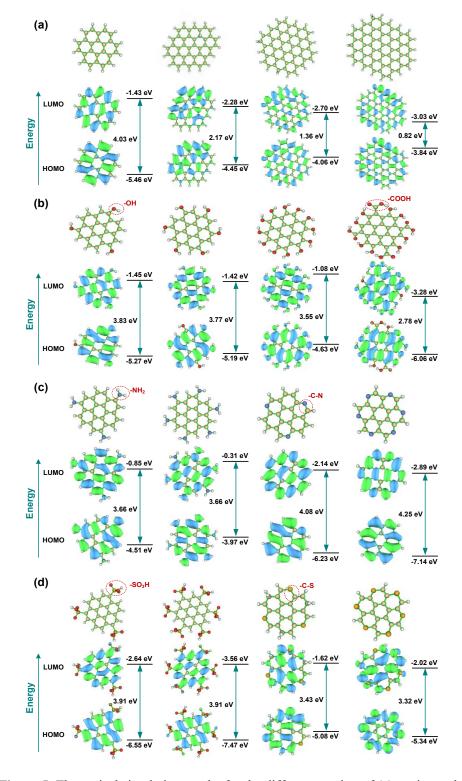**Figure 4.** Schematic illustration of the fluorescence mechanism of G-CQDs and B-CQDs.

Figure 5. Theoretical simulation results for the different number of (a) conjugated rings, (b) oxygen-containing functional groups, (c) nitrogen-containing functional groups and (d) sulfur -containing functional groups.

3.4 Formation mechanism of G-CQDs and B-CQDs

The Raman, FT-IR, and XPS characterization are employed to investigate the evolution of surface structure and chemical composition from AL to CQDs in the synthetic route. According to the Raman spectra of Figure 6a, it can be seen that the D peak of the disordered sp^3 carbon of AL is stronger than the G peak of the graphitized sp^2 carbon, while the SLs almost contain all amorphous carbon, and the graphitic carbon in AL is mostly retained in SRs after acid hydrolysis. The degree of graphitization is significantly enhanced after hydrothermal carbonization according to the increased intensity ratios (I_G/I_D) from ~ 0 of SLs to 0.38 of G-CQDs, and from 0.39 of SRs to 0.58 of B-CQDs. The FT-IR spectra (Figure 6b) show that AL is mainly composed of O-H, C-H, C=C, and C-O functional groups on the surface. The vibration strength of C-O groups decrease markedly, while that of C=O groups increase on the surface of SLs and SRs after acid hydrolysis of AL. Meanwhile, a large number of abundant N-H, C-N, and C-S functional groups appear on the surface of SLs, while SRs retain most of the surface structure of AL in addition to a small amount of N- and S-containing groups. The vibration strengths of O-H, N-H, C-O, C-N, and C-S groups are decreased from SLs to G-CQDs, and SRs to B-CQDs, while those of C=O and C=C groups are increased after the hydrothermal carbonization. The N, S-containing functional groups on the surface of G-CQDs are significantly more abundant than that of B-CQDs. These results can be also evidenced by the high-resolution XPS spectra of AL, SLs and SRs. As displayed in the C 1s and O 1s spectra (Figure 6c and 6d), the content of C-O groups decrease, while the content of C=O groups increase from AL to SLs and SRs during acidolysis. The N 1s spectra in Figure 6e show that the N element is introduced into SLs mainly in the form of amide N groups through the addition

of acids, and a small amount of N is doped into SRs in the form of graphite N groups. The S 2p

spectra in Figure 6f show that the S element is doped into SLs and SRs in the form of C-S and

C-SO$_x$ groups. Furthermore, the quantitative analysis data of XPS is listed in Table 1. After

acid oxidation of AL, the C contents on the surface of SLs and SRs decrease, while the O, N,

and S contents apparently increase. The N and S contents slightly decrease from SLs to G-

CQDs and from SRs to B-CQDs, while the C contents are enhanced during hydrothermal

carbonization. It suggests that the C-O bond of AL is broken during acid hydrolysis, and the

obtained SLs have a large number of active groups (hydroxyl, amino, sulfhydryl and carboxyl
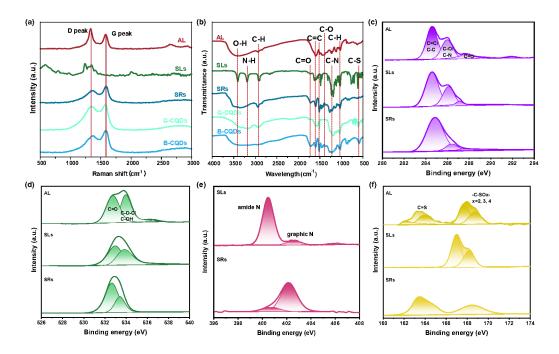
groups) attached on the surface.

Figure 6. (a) Raman spectra, (b) FTIR spectra, and high-resolution XPS spectra of (c) C

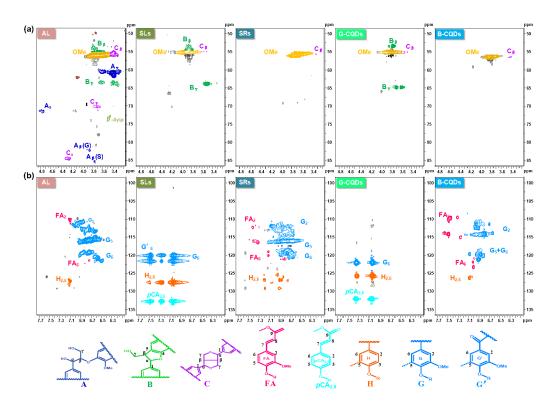1s, (d) O 1s, (e) N 1s, and (f) S 2p of AL, SLs, SRs, G-CQDs, and B-CQDs.

Table 1. The quantitative analysis results of XPS.

sample	C (%)	O (%)	N (%)	S (%)	O/C (%)	N/C (%)	S/C (%)
AL	62.65	35.83	/	1.52	0.57	/	0.02
SLs	40.68	36.92	10.60	11.71	0.91	0.26	0.29
SRs	48.29	42.66	2.95	6.10	0.88	0.06	0.12
G-CQDs	44.75	37.77	7.41	10.07	0.84	0.17	0.23
B-CQDs	51.84	40.11	2.56	5.49	0.77	0.11	0.05

To obtain further comprehensive structural insights on the transformation of lignin during acid hydrolysis and hydrothermal carbonization, AL, SLs, SRs, G-CQDs, and B-CQDs are subjected to 2D- HSQC NMR analysis. Biomass lignin, an aromatic polymer containing a structural unit of phenylpropane connected by ether bonds or C-C bonds, is the most abundant natural macromolecular organic material in the world [49, 50]. The HSQC NMR spectra of the samples exhibit two regions, which are the aliphatic region (δ_C/δ_H: 50–90/3.2–5.0 ppm) (Figure 7a) and the aromatic $^{13}C–^1H$ correlations region (δ_C/δ_H: 100–135/6.0–7.8 ppm) (Figure 7b). The HSQC spectra of AL show plentiful signals at δ_C/δ_H 55.6/3.7, 60.5-82.5/3.3-4.8, 54.1-56.2/3.4-3.6, and 55.4-84.9/3.4-4.3 ppm in the aliphatic region, assigned to the native structure of lignin including methoxyls (OCH_3), β-aryl-ether linkages (A), phenylcoumarane structures (B) and resinol linkages (C), respectively [51]. The signals of ferulate (FA), p-coumarate (pCA), p-hydroxyphenyl (H), guaiacyl units (G) and oxidized guaiacyl units (G') can be apparently observed in the aromatic region at δ_C/δ_H 110.2-126.7/7.1, 126.1/7.1, 132.9/7.1, 114.9-120.9/6.7, and 120.9/7.5 ppm, respectively [52, 53]. The aliphatic signals of A, B, and C structure units are sharply reduced in the HSQC spectra of SLs and almost vanish in that of SRs. This indicates that AL undergoes a strong de-etherification reaction through the cleavage of A, B, and C

linkages under the action of acid hydrolysis, which agrees well with the results of the above

FTIR and XPS analysis. The aromatic structures (FA, H, G, and G') of AL are well inherited

by SRs after the acid hydrolysis. The emerging structure unit of pCA in the HSQC spectra of

SLs may be introduced by the addition of o-aminobenzenesulfonic acid. It suggests that the

bulk of decomposed AL exists in SRs, while the organic fragments of that exist in SLs. The

aliphatic and aromatic structures of G-CQDs and B-CQDs are similar to those of SLs and SRs,

respectively. It demonstrates that the ^{13}C-^{1}H chemical environment exhibits no significant

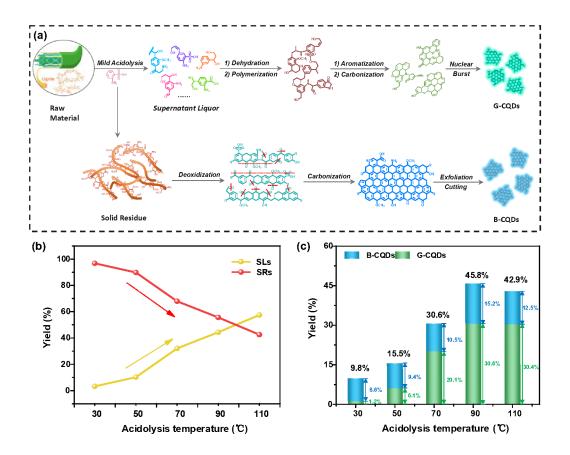change during the hydrothermal carbonization reaction.

Figure 7. (a) The aliphatic structures and (b) aromatic structures identified in the 2D-HSQC NMR spectra of AL, SLs, SRs, G-CQDs, and B-CQDs. (A) β-O-4' linkages, (B) phenylcoumaran with α-O-4' and β-O-5' linkages, (C) resinol with β–β', α-O-γ', and γ-O-α' linkages, (FA) ferulate, (pCA) p-coumarate, (H) p-hydroxyphenyl, (G) guaiacyl units, and (G')

oxidized guaiacyl unit bearing a carbonyl group at Cα.

Based on the experimental evidence above, the possible formation pathway of CQDs by acid hydrolysis-assisted hydrothermal carbonization of AL is proposed in Figure 8a. AL first undergoes deetherization and depolymerization reaction to form SLs and SRs under the action of o-aminobenzenesulfonic acid. The intricate and diverse intermediates formed in the acid hydrolysis. Overall, the water-soluble SLs are mainly composed of small molecular fragments obtained by acid-catalyzed cleavage of ether bonds from AL polymers, while the bulk of AL remains in insoluble SRs. Meanwhile, the N and S atoms from the acid are incorporated on the surfaces of SLs via covalent conjugation, while a relatively small amount of N, S groups exist on the surface of SRs [54]. Notably, o-aminobenzenesulfonic acid acts a triple role as a "top-down" scissor, N, S dopant as well as surfactant during the acidolysis process [55, 56]. It contributes to abundant active sites including –OH, -COOH, and -NH_2 functional groups exposed on the surface of SLs and SRs. In the next step of hydrothermal carbonization, the SLs and SRs serve as precursors for the preparation of G-CQDs and B-CQDs, respectively. The functionalized SLs undergo intermolecular and intramolecular dehydration and condensation among the active -COOH, -OH, and -NH_2 groups. The conjugated molecules are further polymerized, crosslinked, and carbonized under the hydrothermal treatment [57]. With the prolongation of hydrothermal carbonization, the prompt π-π stacking and increased sp^2 hybridization result in the growth of the carbon nucleus [58, 59]. N and S atoms are simultaneously incorporated as C-N, N-H, and C-S groups into the heterocyclic ring systems, resulting in the final formation of the G-CQDs [13]. Different from the bottom-up synthesis of G-CQDs from SLs, SRs are inclined to synthesize B-CQDs via the top-down method due to the fewer active groups on the surface and

large carbon domains inherited from AL. These large carbon domains are reacted with

oxidizing reagents (o-aminobenzenesulfonic acid) for introducing epoxy groups on basal planes

in the acidolysis step. Then the SRs undergo exfoliation and cutting of large carbon domains

followed by deoxidization into small pieces (B-CQDs) in the hydrothermal treatment [2, 60, 61]. In

addition, the effect of the key factor (acidolysis temperature) on production yields of SLs, SRs,

and CQDs is investigated. As shown in Figure 8b and 8c, the yield of SLs increases with

increasing acid hydrolysis temperature from 30 to 110 °C, while the opposite for that of SRs. It

may be attributed to the enhancement of the acidolysis reaction at a higher temperature. The

total production yields of G-CQDs and B-CQDs first increase and then decrease with increasing

acidolysis temperature. The optimal production yield of 45.8% is obtained at the acidolysis

temperature of 90 °C, which is superior to most reported biomass-based CQDs [20-22, 56].

Figure 8. (a) Schematic mechanism for the formation of carbon materials from AL. (b) and (c) Production yields of AL, SLs, SRs, G-CQDs, and B-CQDs at different acidolysis temperatures.

4. Conclusion

A comprehensive utilization strategy is developed to simultaneously produce two kinds of CQDs by mild acidolysis-assisted hydrothermal carbonization of lignin. G-CQDs and B-CQDs are derived from the supernatant and solid residue of acid hydrolyzed lignin, respectively. Compared with B-CQDs, G-CQDs show a higher oxygen degree and have richer sulfur-containing functional groups on the surface, resulting in a red-shift in fluorescence emission from blue to green. The more nitrogen-containing functional groups of G-CQDs lead to a higher QY of 23.7% than that of 5.2% for B-CQDs. The formation pathway of G-CQDs involves the

self-assembly of small organic molecules through a bottom-up process, while that of B-CQDs involves the exfoliation and cutting of large carbon domains via a top-down approach. The total production yield of CQDs is achieved as high as 45.8% by adjusting the acidolysis temperature, which outperforms that of most reported biomass-derived CQDs. This sustainable approach offers enlightening insights for mass production of value-added carbon materials from biomass, and also paves the way for the rational design of complete lignin valorization for "waste-to-wealth".

CRediT authorship contribution statement

Lingli Zhu: Investigation, Methodology, Data curation, Writing-original draft, Validation. Dekui Shen: Conceptualization, Investigation, Writing-original draft, Funding acquisition. Kai Hong Luo: Writing-review, Supervision.

Declaration of Competing Interest

The authors declare that they have no known competing financial interests or personal relationships that could have appeared to influence the work reported in this paper.

Acknowledgements

References

(1)   Liu, H.;   Ding, J.;   Zhang, K.; Ding, L., Construction of biomass carbon dots based fluorescence sensors and their applications in chemical and biological analysis. *Trac-Trends in Analytical Chemistry* **2019**, *118*, 315-337.

(2)   Abbas, A.;   Mariana, L. T.; Phan, A. N., Biomass-waste derived graphene quantum dots and their applications. *Carbon* **2018**, *140*, 77-99.

(3)   Wang, Z.;   Shen, D.;   Wu, C.; Gu, S., State-of-the-art on the production and application of carbon nanomaterials from biomass. *Green Chemistry* **2018,** *20* (22), 5031-5057.

(4)   Zhu, L.;   Shen, D.;   Wu, C.;   Gu, S., State-of-the-Art on the Preparation, Modification, and Application of Biomass-Derived Carbon Quantum Dots. *Industrial & Engineering Chemistry Research* **2020**, *59* (51), 22017-22039.

(5)   Luong, D. X.;   Bets, K. V.;   Algozeeb, W. A.;   Stanford, M. G.;   Kittrell, C.; Chen, W.;   Salvatierra, R. V.;   Ren, M.;   McHugh, E. A.;   Advincula, P. A.;   Wang, Z.; Bhatt, M.;   Guo, H.;   Mancevski, V.;   Shahsavari, R.;   Yakobson, B. I.; Tour, J. M., Gram-scale bottom-up flash graphene synthesis. *Nature* **2020,** *577* (7792), 647-651.

(6)   Wang, Z.;   Qin, K.;   Wang, Z.;   Shen, D.; Wu, C., Carbon nanotubes/Al2O3 composite derived from catalytic reforming of the pyrolysis volatiles of the mixture of polyethylene and lignin for highly-efficient removal of Pb(ii). *RSC Advances* **2021,** *11* (60), 37851-37865.

(7)   Yu, B.;   Gele, A.; Wang, L., Iron oxide/lignin-based hollow carbon nanofibers nanocomposite as an application electrode materials for supercapacitors. *Int J Biol Macromol* **2018,** *118* (Pt A), 478-484.

(8)   Wu, X.;   Guo, T.;   Chen, Z.;   Wang, Z.;   Qin, K.;   Wang, Z.;   Ao, Z.;   Yang, C.; Shen, D.; Wu, C., Facile and green preparation of solid carbon nanoonions via catalytic co-pyrolysis of lignin and polyethylene and their adsorption capability towards Cu(ii). *RSC Advances* **2022,** *12* (8), 5042-5052.

(9)   Zhu, L.;   Shen, D.; Luo, K. H., A critical review on VOCs adsorption by different porous materials: Species, mechanisms and modification methods. *J Hazard Mater* **2020,** *389*, 122102.

(10)   Zhu, L.;   Shen, D.;   Wang, Q.; Luo, K. H., Green Synthesis of Tunable Fluorescent Carbon Quantum Dots from Lignin and Their Application in Anti-Counterfeit Printing. *ACS Applied Materials & Interfaces* **2021**.

(11)   Shen, D.;   Jin, W.;   Hu, J.;   Xiao, R.; Luo, K., An overview on fast pyrolysis of the main constituents in lignocellulosic biomass to valued-added chemicals: Structures, pathways and interactions. *Renewable and Sustainable Energy Reviews* **2015,** *51*, 761-774.

(12)   Brachi, P., Synthesis of carbon dots (CDs) through the fluidized bed thermal treatment of residual biomass assisted by gamma-alumina. *Applied Catalysis B-Environmental* **2020,** *263*.

(13)   Jing, S.;   Zhao, Y.;   Sun, R.-C.;   Zhong, L.; Peng, X., Facile and High-Yield Synthesis of Carbon Quantum Dots from Biomass-Derived Carbons at Mild Condition. *Acs Sustainable Chemistry & Engineering* **2019,** *7* (8), 7833-7843.

(14)   Cailotto, S.;   Mazzaro, R.;   Enrichi, F.;   Vomiero, A.;   Selva, M.;   Cattaruzza, E.; Cristofori, D.;   Amadio, E.; Perosa, A., Design of Carbon Dots for Metal-free Photoredox Catalysis. *Acs Applied Materials & Interfaces* **2018,** *10* (47), 40560-40567.

(15)   Shen, J.;   Shang, S.;   Chen, X.;   Wang, D.; Cai, Y., Highly fluorescent N, S-co-doped carbon dots and their potential applications as antioxidants and sensitive probes for Cr (VI) detection. *Sensors and Actuators B: Chemical* **2017,** *248*, 92-100.

(16)   Liang, Q.;   Ma, W.;   Shi, Y.;   Li, Z.; Yang, X., Easy synthesis of highly fluorescent carbon quantum dots from gelatin and their luminescent properties and applications. *Carbon* **2013,** *60*, 421-428.

(17)   Zhu, P.;   Li, J.;   Gao, L.;   Xiong, J.;   Tan, K., Strategy to Synthesize Tunable Multiemission Carbon Dots and Their Multicolor Visualization Application. *ACS Appl Mater Interfaces* **2021,** *13* (28), 33354-33362.

(18)   Zheng, Y.;   Arkin, K.;   Hao, J.;   Zhang, S.;   Guan, W.;   Wang, L.;   Guo, Y.;   Shang, Q., Multicolor Carbon Dots Prepared by Single‐Factor Control of Graphitization and Surface Oxidation for High-Quality White Light-Emitting Diodes. *Advanced Optical Materials* **2021**.

(19)   Yang, P.;   Zhu, Z.;   Zhang, T.;   Chen, M.;   Cao, Y.;   Zhang, W.;   Wang, X.;   Zhou, X.; Chen, W., Facile synthesis and photoluminescence mechanism of green emitting xylose-derived carbon dots for anti-counterfeit printing. *Carbon* **2019,** *146*, 636-649.

(20)   Guo, L.-P.;   Zhang, Y.; Li, W.-C., Sustainable microalgae for the simultaneous synthesis of carbon quantum dots for cellular imaging and porous carbon for CO2 capture. *Journal of Colloid and Interface Science* **2017,** *493*, 257-264.

(21)   Zhang, H.;   Chen, J.;   Li, Y.;   Liu, P.;   Wang, Y.;   An, T.; Zhao, H., Nitrogen-Doped Carbon Nanodots@Nanospheres as An Efficient Electrocatalyst for Oxygen Reduction Reaction. *Electrochimica Acta* **2015,** *165*, 7-13.

(22)   Alam, A.-M.;   Park, B.-Y.;   Ghouri, Z. K.;   Park, M.;   Kim, H.-Y., Synthesis of carbon quantum dots from cabbage with down- and up-conversion photoluminescence properties: excellent imaging agent for biomedical applications. *Green Chemistry* **2015,** *17* (7), 3791-3797.

(23)   Jones, S. S.;   Sahatiya, P.;   Badhulika, S., One step, high yield synthesis of amphiphilic carbon quantum dots derived from chia seeds: a solvatochromic study. *New Journal of Chemistry* **2017,** *41* (21), 13130-13139.

(24)   Liang, Z.;   Kang, M.;   Payne, G. F.;   Wang, X.;   Sun, R., Probing Energy and Electron Transfer Mechanisms in Fluorescence Quenching of Biomass Carbon Quantum Dots. *Acs Applied Materials & Interfaces* **2016,** *8* (27), 17478-17488.

(25)   Chai, X.;   He, H.;   Fan, H.;   Kang, X.;   Song, X., A hydrothermal-carbonization process for simultaneously production of sugars, graphene quantum dots, and porous carbon from sugarcane bagasse. *Bioresource Technology* **2019,** *282*, 142-147.

(26)   Wang, Z.;   Yu, J.;   Zhang, X.;   Li, N.;   Liu, B.;   Li, Y.;   Wang, Y.;   Wang, W.;   Li, Y.;   Zhang, L.;   Dissanayake, S.;   Suib, S. L.; Sun, L., Large-Scale and Controllable Synthesis of Graphene Quantum Dots from Rice Husk Biomass: A Comprehensive Utilization Strategy. *Acs Applied Materials & Interfaces* **2016,** *8* (2), 1434-1439.

(27)   Zhou, Y.;   Liu, Y.;   Li, Y.;   He, Z.;   Xu, Q.;   Chen, Y.;   Street, J.;   Guo, H.;   Nelles, M., Multicolor carbon nanodots from food waste and their heavy metal ion detection application. *Rsc Advances* **2018,** *8* (42), 23657-23662.

(28)   Zhao, Y.;   Jing, S.;   Peng, X.;   Chen, Z.;   Hu, Y.;   Zhuo, H.;   Sun, R.; Zhong, L., Synthesizing green carbon dots with exceptionally high yield from biomass hydrothermal

carbon. *Cellulose* **2019**.

(29)   Li, F.;   Li, Y.;   Yang, X.;   Han, X.;   Jiao, Y.;   Wei, T.;   Yang, D.;   Xu, H.; Nie, G., Highly Fluorescent Chiral N-S-Doped Carbon Dots from Cysteine: Affecting Cellular Energy Metabolism. *Angewandte Chemie-International Edition* **2018**, *57* (9), 2377-2382.

(30)   Zhang, H.;   Kang, S.;   Wang, G.;   Zhang, Y.;   Zhaou, H., Fluorescence Determination of Nitrite in Water Using Prawn-Shell Derived Nitrogen-Doped Carbon Nanodots as Fluorophores. *Acs Sensors* **2016,** *1* (7), 875-881.

(31)   Zhang, B.;   Liu, Y.;   Ren, M.;   Li, W.;   Zhang, X.;   Vajtai, R.;   Ajayan, P. M.; Tour, J. M.; Wang, L., Sustainable Synthesis of Bright Green Fluorescent Nitrogen-Doped Carbon Quantum Dots from Alkali Lignin. *Chemsuschem* **2019,** *12* (18), 4202-4210.

(32)   Ding, H.;   Wei, J.-S.;   Zhang, P.;   Zhou, Z.-Y.;   Gao, Q.-Y.;   Xiong, H.-M., Solvent-Controlled Synthesis of Highly Luminescent Carbon Dots with a Wide Color Gamut and Narrowed Emission Peak Widths. *Small* **2018,** *14* (22).

(33)   Zhao, Y.;   Ou, C.;   Yu, J.;   Zhang, Y.;   Song, H.;   Zhai, Y.; Tang, Z.; Lu, S., Facile Synthesis of Water-Stable Multicolor Carbonized Polymer Dots from a Single Unconjugated Glucose for Engineering White Light-Emitting Diodes with a High Color Rendering Index. *ACS Appl Mater Interfaces* **2021**.

(34)   Wang, J.;   Li, Q.;   Zheng, J.;   Yang, Y.;   Liu, X.; Xu, B., N, B-Codoping Induces High-Efficiency Solid-State Fluorescence and Dual Emission of Yellow/Orange Carbon Dots. *ACS Sustainable Chemistry & Engineering* **2021,** *9* (5), 2224-2236.

(35)   Jia, M.;   Peng, L.;   Yang, M.;   Wei, H.;   Zhang, M.; Wang, Y., Carbon dots with dual emission: A versatile sensing platform for rapid assay of Cr (VI). *Carbon* **2021,** *182*, 42-50.

(36)   Tian, T.;   He, Y.;   Ge, Y.; Song, G., One-pot synthesis of boron and nitrogen co-doped carbon dots as the fluorescence probe for dopamine based on the redox reaction between Cr(VI) and dopamine. *Sensors and Actuators B: Chemical* **2017,** *240*, 1265-1271.

(37)   Wang, B.;   Song, H.;   Tang, Z.;   Yang, B.; Lu, S., Ethanol-derived white emissive carbon dots: the formation process investigation and multi-color/white LEDs preparation. *Nano Research* **2021**.

(38)   Macairan, J. R.;   de Medeiros, T. V.;   Gazzetto, M.;   Yarur Villanueva, F.; Cannizzo, A.; Naccache, R., Elucidating the mechanism of dual-fluorescence in carbon dots. *J Colloid Interface Sci* **2021,** *606* (Pt 1), 67-76.

(39)   Zhu, P.;   Tan, K.;   Chen, Q.;   Xiong, J.; Gao, L., Origins of Efficient Multiemission Luminescence in Carbon Dots. *Chemistry of Materials* **2019,** *31* (13), 4732-4742.

(40)   Zhu, Z.;   Yang, P.;   Li, X.;   Luo, M.;   Zhang, W.;   Chen, M.; Zhou, X., Green preparation of palm powder-derived carbon dots co-doped with sulfur/chlorine and their application in visible-light photocatalysis. *Spectrochimica Acta Part a-Molecular and Biomolecular Spectroscopy* **2020,** *227*.

(41)   Liao, X.;   Chen, C.;   Zhou, R.;   Huang, Q.;   Liang, Q.;   Huang, Z.;   Zhang, Y.; Hu, H.; Liang, Y., Comparison of N-doped carbon dots synthesized from the main components of plants including cellulose, lignin, and xylose: Characterized, fluorescence mechanism, and potential applications. *Dyes and Pigments* **2020,** *183*.

(42)   Yuan, Y. H.;   Liu, Z. X.;   Li, R. S.;   Zou, H. Y.;   Lin, M.;   Liu, H.; Huang, C. Z., Synthesis of nitrogen-doping carbon dots with different photoluminescence properties by

controlling the surface states. *Nanoscale* **2016,** *8* (12), 6770-6776.

(43)   Chen, Y.; Lian, H.; Wei, Y.; He, X.; Chen, Y.; Wang, B.; Zeng, Q.; Lin, J., Concentration-induced multi-colored emissions in carbon dots: origination from triple fluorescent centers. *Nanoscale* **2018,** *10* (14), 6734-6743.

(44)   Ferreyra, D. D.; Rodríguez Sartori, D.; Ezquerra Riega, S. D.; Rodríguez, H. B.; Gonzalez, M. C., Tuning the nitrogen content of carbon dots in carbon nitride nanoflakes. *Carbon* **2020,** *167*, 230-243.

(45)   Zhang, Y.; Qin, H.; Huang, Y.; Zhang, F.; Liu, H.; Liu, H.; Wang, Z. J.; Li, R., Highly fluorescent nitrogen and boron doped carbon quantum dots for selective and sensitive detection of Fe3+. *Journal of Materials Chemistry B* **2021,** *9* (23), 4654-4662.

(46)   Liu, Y.; Li, W.; Wu, P.; Ma, C.; Wu, X.; Xu, M.; Luo, S.; Xu, Z.; Liu, S., Hydrothermal synthesis of nitrogen and boron co-doped carbon quantum dots for application in acetone and dopamine sensors and multicolor cellular imaging. *Sensors and Actuators B: Chemical* **2019,** *281*, 34-43.

(47)   Shi, Y.; Liu, X.; Wang, M.; Huang, J.; Jiang, X.; Pang, J.; Xu, F.; Zhang, X., Synthesis of N-doped carbon quantum dots from bio-waste lignin for selective irons detection and cellular imaging. *International Journal of Biological Macromolecules* **2019,** *128*, 537-545.

(48)   Sk, M. A.; Ananthanarayanan, A.; Huang, L.; Lim, K. H.; Chen, P., Revealing the tunable photoluminescence properties of graphene quantum dots. *J. Mater. Chem. C* **2014,** *2* (34), 6954-6960.

(49)   Zhu, C.; Dou, X.; Li, W.; Liu, X.; Li, Q.; Ma, J.; Liu, Q.; Ma, L., Efficient depolymerization of Kraft lignin to liquid fuels over an amorphous titanium-zirconium mixed oxide supported partially reduced nickel-cobalt catalyst. *Bioresour Technol* **2019,** *284*, 293-301.

(50)   Zhu, J.; Chen, F.; Zhang, Z.; Li, M.; Yang, Q.; Yang, Y.; Bao, Z.; Ren, Q., M-Gallate (M = Ni, Co) Metal–Organic Framework-Derived Ni/C and Bimetallic Ni–Co/C Catalysts for Lignin Conversion into Monophenols. *ACS Sustainable Chemistry & Engineering* **2019,** *7* (15), 12955-12963.

(51)   Luo, H.; Abu-Omar, M. M., Lignin extraction and catalytic upgrading from genetically modified poplar. *Green Chemistry* **2018,** *20* (3), 745-753.

(52)   Zhao, W.; Xiao, L.-P.; Song, G.; Sun, R.-C.; He, L.; Singh, S.; Simmons, B. A.; Cheng, G., From lignin subunits to aggregates: insights into lignin solubilization. *Green Chemistry* **2017,** *19* (14), 3272-3281.

(53)   Wang, M.; Lu, J.; Zhang, X.; Li, L.; Li, H.; Luo, N.; Wang, F., Two-Step, Catalytic C–C Bond Oxidative Cleavage Process Converts Lignin Models and Extracts to Aromatic Acids. *ACS Catalysis* **2016,** *6* (9), 6086-6090.

(54)   Wang, R.; Xia, G.; Zhong, W.; Chen, L.; Chen, L.; Wang, Y.; Min, Y.; Li, K., Direct transformation of lignin into fluorescence-switchable graphene quantum dots and their application in ultrasensitive profiling of a physiological oxidant. *Green Chemistry* **2019,** *21* (12), 3343-3352.

(55)   Wang, R.; Jiao, L.; Zhou, X.; Guo, Z.; Bian, H.; Dai, H., Highly fluorescent graphene quantum dots from biorefinery waste for tri-channel sensitive detection of Fe3+ ions. *Journal of hazardous materials* **2021,** *412*, 125096-125096.

(56)   Ding, Z.; Li, F.; Wen, J.; Wang, X.; Sun, R., Gram-scale synthesis of single-crystalline graphene quantum dots derived from lignin biomass. *Green Chemistry* **2018,** *20* (6),

1383-1390.

(57)   Wang, J.; Zhang, P.; Huang, C.; Liu, G.; Leung, K. C.; Wang, Y. X., High Performance Photoluminescent Carbon Dots for In Vitro and In Vivo Bioimaging: Effect of Nitrogen Doping Ratios. *Langmuir* **2015,** *31* (29), 8063-73.

(58)   Zhu, L.; Shen, D.; Liu, Q.; Wu, C.; Gu, S., Sustainable synthesis of bright green fluorescent carbon quantum dots from lignin for highly sensitive detection of Fe3+ ions. *Applied Surface Science* **2021,** *565*.

(59)   Si, M.; Zhang, J.; He, Y.; Yang, Z.; Yan, X.; Liu, M.; Zhuo, S.; Wang, S.; Min, X.; Gao, C.; Chai, L.; Shi, Y., Synchronous and rapid preparation of lignin nanoparticles and carbon quantum dots from natural lignocellulose. *Green Chemistry* **2018,** *20* (15), 3414-3419.

(60)   Lim, S. Y.; Shen, W.; Gao, Z., Carbon quantum dots and their applications. *Chemical Society Reviews* **2015,** *44* (1), 362-381.

(61)   Wang, Y.; Hu, A., Carbon quantum dots: synthesis, properties and applications. *Journal of Materials Chemistry C* **2014,** *2* (34).